Journal of Physics Communications

PAPER

Decoherence of a spin-valley qubit in a MoS_2 quantum dot

Mehdi Arfaoui[1] and **Sihem Jaziri**[1,2]

[1] Laboratoire de Physique de la Matière Condensée, Département de Physique, Faculté des Sciences de Tunis, Université Tunis El Manar, Campus Universitaire 1060 Tunis, Tunisia
[2] Laboratoire de Physique des Matériaux, Faculté des Sciences de Bizerte, Université de Carthage, 7021 Jarzouna, Tunisia

E-mail: mehdi.arfaoui@fst.utm.tn

Keywords: quantum dots, quantum master equation, decoherence, spin dynamics, quantum information with solid state qubits, noise, open quantum systems

OPEN ACCESS

RECEIVED
4 August 2022

REVISED
27 October 2022

ACCEPTED FOR PUBLICATION
14 November 2022

PUBLISHED
24 November 2022

Abstract

Transition metal dichalcogenide (TMD)-based quantum dots (QDs) have proven to be a successful and promising device for physically implementing electron spin-valley based qubits. Although the electron spin in a TMDs monolayer semiconductor QD can be isolated and controlled with high precision, decoherence occurs due to unavoidable coupling with the surrounding environment, such as nuclear spin environments. In this paper, using an exact master equation (ME) of spin qubit dynamics coupled to a nuclear spin bath in terms of hyperfine interaction (HI), we have investigated the controllability of dynamics processes with varying degrees of non-Markovianity. In large magnetic fields, we show that pure spin or valley qubits can be created. We calculate the loss of fidelity due to the Overhauser field of HI in a wide range of nuclear spin $\mathcal{N}$. In this context, we prove that this field restricts the decoherence process of the central electron spin, which can regain its coherence. Finally, we discuss how the coherence of the spin qubit remains robust for large $\mathcal{N}$.

1. Introduction

Modern life is fueled by data, which drives the demand for computational power to the point where new generations of semiconductor technology are constantly being deployed. Several publications since then have focused on improving and developing valleytronic devices [1, 2], and transition metal dichalcogenide (TMD) qubits, including valley qubits, spin qubits, spin-valley qubits, and even impurity-based qubits [3–9]. TMD-based quantum dots (QDs) have attracted significant attention due to their potential applications in optoelectronics [10–13] including light sensors [14], logic circuits [15, 16] and valleytronics [17–20]. Recently, MoS_2-QDs have gained attention as a novel qubit pattern with potential for future quantum devices. However, the decoherence on this system is seen as a significant barrier to the deployment of quantum devices. The major obstacles addressed pose a challenge to researchers because noise hinders the transmission of quantum signals. One of the essential tools in the study of spin-valley qubits in QDs is stability, which is sensitive to disturbances of a noisy environment. Indeed, the inevitable coupling with their environment quickly destroys the phase relations (superposition of incompatible states) between the quantum states until they become classical states. The electron spin in a QD has two main decoherence channels: (i) (Markovian) phonon-assisted relaxation channel, due to the presence of spin-orbit interaction, (ii) (non-Markovian) spin bath constituted by the spins of the nuclei in the QD that interact with the electron spin via the hyperfine interaction (HI) [6, 21–26] where the number of nuclear spins varies between $\sim 10^2$ and 10^6. In our case, the calculations are carried out at zero temperature, so that phonon absorption and multi-phonon processes are negligible [6, 27]. Full polarized baths are employed to facilitate qubit operations and extend coherence times [28]. Theoretically, it has been suggested as the storage of an electron spin state in a paper by Kurucz *et al* [29]. In straightforward experimental setups, a spin bath is polarized by manipulating a single qubit [23, 30–32], whose polarization can be reset repeatedly.

The central spin model, which entails a central spin interacting with many surrounding spins, can be used to describe realistic quantum many-spin systems, including the semiconductor quantum dots [33, 34], the nitrogen-vacancy center in the diamond [35, 36], and others. These solid-state central spin systems have recently

Table 1. Nuclear g-factor for different isotopes, that allowing non-zero nuclear spin, and nuclear Zeeman splitting in a magnetic field $b_z \sim 1.5 \times 10^{-2}$T for MoS_2. Note that $|\omega_s| = (10^3 \sim 10^4)|\omega_k|$, as for the nuclear spin frequencies ω_k, their magnitudes are three-order smaller than ω_s.

Isotopes	^{95}Mo	^{97}Mo	^{33}S
g_I	−0.3657	-0.3734	0.4292
$\lvert\omega_k\rvert = \lvert g_I \mu_N b_z\rvert$ [$10^{-3} \times \mu$eV]	0.17	0.18	0.2

received a lot of attention from researchers working in quantum information, quantum computation [34, 37], quantum metrology, and quantum sensing [38–40]. In this context, a dynamic framework describes how to suppress HI-induced decoherence using the second-order time-convolutionless (TCL) master equation (ME) method [41–50], which is an effective method for dealing with such systems, was proposed [51]. This work inspired us to seek a dynamic scheme of spin qubit system in order to achieve high fidelity. We apply our theory to the prototypical model system for the spin-valley qubit hosted by MoS_2-QD proposed by Kormányos *et al* [3].

In this paper, we use the TCL ME to solve the central spin problem. This equation enables us to study the dynamics of the central spin, and more interestingly to show the fidelity of the spin qubit to investigate the non-Markovian signature in the dynamical decoherence of open quantum systems. In response to this idea, we examine a precisely solvable decoherence phenomenon at a MoS_2-QD qubit system in a fluctuating environment with fully polarized nuclear spins.

The paper is organized as follows. In section 2 we derive an effective Hamiltonian describing this single-electron spin and $\mathcal{N}$ spin nuclei in interaction. Our approach is based on deriving an appropriate exact non-Markovian TCL ME describing the evolution of the qubit system. We further apply this result to quantify the fidelity loss that noise induces. In the final section, we discuss and conclude our findings.

2. Master equation of an electron spin in MoS_2-QD

Our major aim is to study the HI-induced decoherence in a prototype model system for the spin-valley qubit hosted by MoS_2-QD for the states $|0\rangle = |K', \downarrow\rangle, |1\rangle = |K', \uparrow\rangle$. In appendix A, the proper choice of the spin-valley qubit is discussed in detail. We assume that the initial energy of this problem is the total energy of the desired spin-valley qubits $\mathcal{E}_{0,0}^{K',\downarrow}$ and the surrounding nuclei within the MoS_2-QD after the appropriate magnetic field is applied $\omega_i = g_{I_k}\mu_N B_z^c$, which may be set as origin. In this case, the electron wavefunction is localized within a QD with $R = 26$ nm. The effective Hamiltonian for single-electron spin with a bath of a $\mathcal{N}$ spin-I_0 nuclei, through the contact HI, in a magnetic field b_z along the z-axis, given by (setting $\hbar = 1$),

$$\mathcal{H}_{\rm tot} = \omega_s S_z + \omega_k I_z + \mathbf{h}.\mathbf{S} \tag{1}$$

where $\mathbf{S} = (S_x, S_y, S_z)$ is the electron spin operator. $\omega_s = g_{sp}\mu_B b_z$ ($\omega_k = g_{I_k}\mu_N b_z$) is the electron (nuclear) Zeeman splitting in a magnetic field b_z, with an effective g-factor g_{sp} (g_I) for the electron (nuclei) and Bohr (nuclear) magneton $\mu_B \sim 2000\ \mu_N$ (μ_N), see table 1.

In equation (1), we have neglected the anisotropic HI, electron-electron interaction, dipole-dipole interaction between nuclear spins, and nuclear quadrupolar splitting [52, 53]. Appendix C contains detailed calculations of this approximation. The overall activity of a $\mathcal{N}$ nuclear spin environment can be understood as a nuclear magnetic field. This is later called the Overhauser field [33, 54–57] $\mathbf{h} = (h_x, h_y, h_z) = \sum_{k=0}^{\mathcal{N}-1} A_k \mathbf{I}_k$ where $\mathbf{I}_k = (I_k^x, I_k^y, I_k^z)$ is the nuclear spin operator at the lattice site k at position $\mathbf{r}_k$. $I_z = \Sigma_k I_k^z$ is the total z component of nuclear spin and A_k is the associated hyperfine coupling constant. We also introduced the raising and lowering operators $S_\pm = S_x \pm iS_y$ and $I_k^\pm = I_k^x \pm iI_k^y$ respectively, and the nuclear magnetic field operators $h^\pm = h_x \pm ih_y$. Therefore, we can rewrite equation (1) as follows:

$$\mathcal{H}_{\rm tot} = \omega_s S_z + \sum_k \omega_k I_k^z + \sum_k \frac{A_k}{2}(S_+ I_k^- + S_- I_k^+) + \sum_k A_k S_z I_k^z \tag{2}$$

The third and the fourth terms in equation (2) are the hyperfine contact interaction between the spin electron and the nuclei in the QD, which describe the flip-flop interaction and (longitudinal) Overhauser's field, giving rise to the inhomogeneous broadening and dephasing, indeed the last term, $\sum_k A_k S_z I_z^k$, produces an effective magnetic field for the electron $B_{\rm eff} = b_z - \mathcal{B}_N$, where [23] $\mathcal{B}_N = \sum_k A_k I_z^k / (g_{sp}\mu_B)$. As a result, the well-known Overhauser shift occurs. However, when $g_{sp}\mu_B B_{\rm eff} \ll (\sum_k A_k / 2(S_+ I_k^- + S_- I_k^+))$, the spin exchange becomes the dominant effect [37]. The strength $A_k = A^{i_k} v_0 |\psi_{0,0}^{K',s}(\mathbf{r}_k)|^2$ is determined by the electron density at the nuclei site [58], which corresponds to the HI of an electron with nuclear spin at the site k with position r_k. Here, $v_0 = \sqrt{3}\ a^2/4$ is the two-dimensional volume of a unit cell containing one nucleus, and a is the lattice

Table 2. Comparison of the most important parameters of GaAs, Graphene(^{13}C) and MoS_2. The main isotopes that allowing non-zero nuclear spin, the total number of nuclei $\mathcal{N}_{\rm tot}$ estimated for a QD of typical size $R = 26$ nm, the hyperfine strength A and the timescale $\tau_{HF} \sim 2\hbar\mathcal{N}/\nu A$ [22, 61] for the decay of the electron spin due to the contact HI.

	Units		GaAs		^{13}C		MoS_2	
Main Isotopes	[1]	^{71}Ga	^{69}Ga	^{75}As	^{13}C	^{95}Mo	^{97}Mo	^{33}S
$\mathcal{N}_{\rm tot}$	[1]		15×10^3		8×10^4		5×10^4	
Abundance δ_i	[1]	39.89%	60.10%	100%	1.07%	15.92%	9.55%	0.76%
$\mathcal{N}$	[1]		15×10^3		8×10^2		10^4	
A^i	[μeV]	96 [60]	74 [60]	86 [60]	0.6 [22]	−0.57 [61]	−0.57 [61]	0.75 [61]
I_0	[1]	3/2	3/2	3/2	1/2	5/2	5/2	3/2
$\tau_{HF\propto\hbar/A}$	[μs]		0.2		178		219	
$\tau_{SW} \sim 2\pi\hbar/A$	[ns]		5.10^{-2}		7		14	

parameter. For MoS_2-QD of size $R = 26$ nm with a lattice constant given by a = 3.19 Å, there are $\mathcal{N}_{tot} = \pi R^2/v_0 \sim 10^4$ nuclei within the dot. However, only the isotopes that allow nonzero nuclear spin will be part of these nuclei, ^{95}Mo, ^{97}Mo and ^{33}S. Furthermore, the concentration of ^{33}S is negligible compared to that of Mo isotopes, and the decoherence of the electron spin mainly originates from the presence of ^{95}Mo and ^{97}Mo nuclear spins [59]. This leads to the number of nuclear spins within the QD, $\mathcal{N} = (\sum_i \delta_i)\mathcal{N}_{tot}$, where δ_i is the natural abundance for different nuclear isotopic species *i*. $\psi^{K',s}_{0,0}(\mathbf{r}_k)$ is the envelope wavefunction of the localized electron, and $A^{i_k} = -\frac{\mu_0}{4\pi} \cdot \frac{8\pi}{3}\gamma_S\gamma_{i_k}|u_{i_k}|^2$ is the total hyperfine coupling constant to a nuclear spin of species i_k at site k [55]. μ_0 is the vacuum permeability. u_{i_k} is the amplitude of the periodic part of the Bloch function at the position of the nucleus of i_k species. γ_S is the gyromagnetic ratio of free electrons, and its value is always negative. However, the nuclear gyromagnetic ratio γ_{i_k} can take either sign. As a result, the hyperfine coupling constant A^{i_k} might be positive or negative. For convenience, in a material containing several nuclear isotopic species, i_k, we define an average hyperfine coupling constant. Here, we take the root-mean-square (RMS) average [52, 60], $A = \sqrt{\sum_i \delta_i (A^i)^2}$. For MoS_2, the hyperfine constant estimated for ^{95}Mo and ^{97}Mo is $A^{^{95}\rm Mo} = A^{^{97}\rm Mo} = -0.57$ μeV [61], by using these coupling constants with the abundances listed in table 2 gives an RMS coupling strength A = 0.29 μeV. To show the isotopes that contribute the most to HI decoherence in MoS_2, we depict in figure 1(a) the decoherence rate $1/T_2 = \Gamma = \sum_i \Gamma_i$, where it is theoretically demonstrated in the work of Coish *et al* [52]

$$\Gamma_i = \frac{1}{T_2^i} = \delta_i^2 \frac{\pi}{3}\left(\frac{I_i(I_i+1)A^i}{3\,\omega_s}\right)^2 \frac{A^i}{\mathcal{N}} \tag{3}$$

Γ_i is the contribution of flip-flops between the nuclei of common species *i*. Figure 1(a) displays the decay rates for a MoS_2-QD; the Mo isotopes have the greatest influence, whilst the S isotopes are negligible. The quadratic dependence on isotopic abundance δ_i, shown in equation (3), is particularly an important factor in the decoherence rate. Due to this dependence, electron spins in MoS_2 will show decay mainly due to flip-flops between Mo spins, notably ^{95}Mo. Significantly, we can notice relatively high flip-flop rates for the Mo isotopes, as a result of a large nuclear spin 5/2 and isotopic natural abundance, respectively. Here, we considered isotopically purified Mo. It is possible to raise the T_2 of a single layer MoS_2 by performing isotopic purification [59]. Reduction of this noise is possible by fabricating devices using isotopically purified silicon [59, 62]. Moreover, the decoherence time T_2 in MoS_2-QD is several hundreds of *ns*, which is serval orders larger than the operation time in the optical quantum control of spin-valley qubits. Indeed, the coherence time increases with the number of nuclear spin N within the dot size R. For instance, in the MoS_2 crystal's conduction electron, $T_2 = 307$ ns for N = 1000 and $T_2 = 97$ ns for N = 100 [6]. We also notice that T_2 rises with fewer layers, although for MoS_2, the enhancement for a single layer is only two times that of the bulk [59]. Additionally, according to the author J Pawłowski [63], the spin-valley qubit MoS_2 SWAP operations have the lowest fidelity, with a maximum time of 2 ns for 99%-fidelity. Compared to coherence time, operations should last substantially shorter. According to the hyperfine interaction decoherence from Mo nuclear spins, the electron spin-valley degrees of freedom in the MoS_2 monolayer have an estimated coherence time of 100 ns.

Now, we consider a localized electron in its orbital ground state. For a MoS_2-QD with parabolic confinement, the wavefunction for the ground state of a single electron isolated in the CB near the valley K' under a magnetic field reads as follows

$$\psi^{K',s}_{0,0}(r_k) = \frac{1}{\sqrt[4]{\pi}\,\ell_0} exp\left(-\frac{1}{2}\left(\frac{r_k}{\ell_0}\right)^2\right)\chi_s(\sigma_s) \tag{4}$$

where $\ell_0 = \sqrt{\hbar/(2m^{K',s}_{eff}\Omega_{K',s})}$ is the effective length scale equal to the magnetic length $\ell_B = (\hbar/(eB_z))^2$ in the absence of the confining potential ($\omega_0 \to 0$). $\tau = -1$ for K' valley (see discussion of section A), therefore, the ground state wavefunction that will be considered for this work is $\psi^{K',s}_{0,0}(r_k)$.

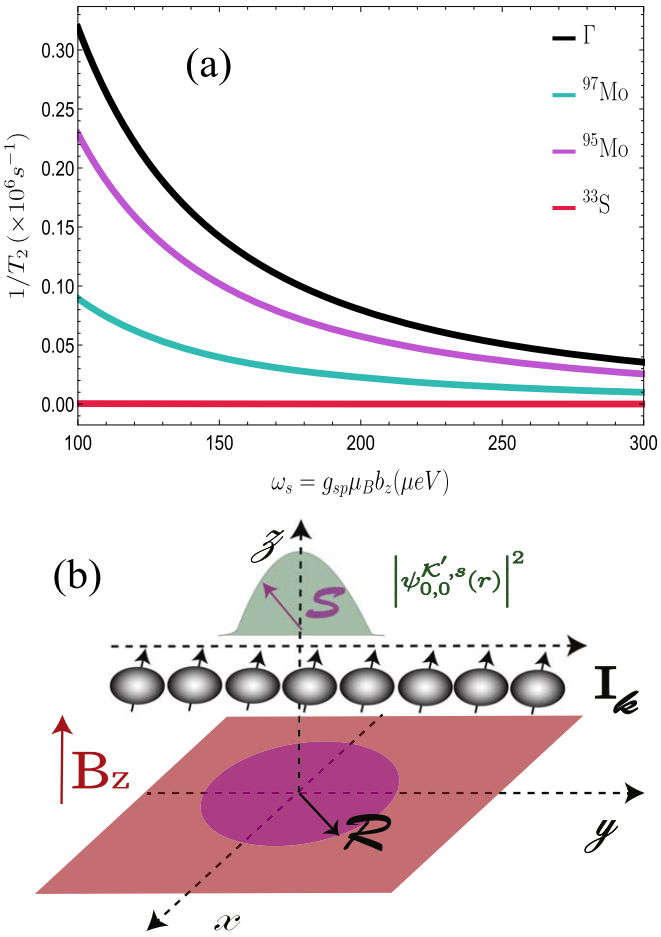

Figure 1. (a) Decay rates for an MoS_2-QD. We utilized $\mathcal{N} = 10^4$ and values from the table 2 for the abundance δ_i and hyperfine constants A^i for MoS_2. (b) Schematic illustration of a two-dimensional MoS_2 QD. An electron spin S is localized in the orbital ground state of the QD, where it is immersed with a full polarized bath of nuclear spins I_k. Due to the confinement, the spatial distribution of the electron in the ground state of the QD is described by a Gaussian envelope function $\psi^{K',s}_{0,0}(r)$ given in equation (4), which in turn leads to a non-uniform HI between the electron spin and the nuclear spins. An external magnetic field is applied perpendicular (B_z) to the plane of the dot (x, y).

Adding and subtracting $\sum_k A_k I_k^z/2$ to the total Hamiltonian

$$\mathcal{H}_{\rm tot} = \omega_s S_z + \sum_k (\omega_k - \frac{A_k}{2}) I_k^z + \sum_k \frac{A_k}{2}(S_+ I_k^- + S_- I_k^+) + \sum_k A_k (S_z + \frac{1}{2}) I_k^z \tag{5}$$

Equation (5) can be split into two main parts, an unperturbed part (longitudinal) represented by the first two terms, which consist of all Zeeman terms, and a perturbation part (transverse) containing the virtual flip-flop processes of the HI. In the interaction picture with respect to the unperturbed part, we can write

$$\begin{aligned} \mathcal{H}^I_{tot} &= e^{i\mathcal{H}_0 t}\mathcal{H}_1 e^{-i\mathcal{H}_0 t} \\ &= \underbrace{S_+(t)h^-(t) + S_-(t)h^+(t)}_{\rm TransversalHyperfineTerm} + \underbrace{|1\rangle\langle 1|h^z}_{\rm Longitudinal} \end{aligned} \tag{6}$$

where $h^{\pm}(t) = \sum_k \frac{A_k}{2} I_k^{\pm} e^{\pm i(\omega_k - A_k/2)t}, S_{\pm}(t) = S_{\pm} e^{\pm i\omega_s t}$ and $h^z = \sum_k A_k I_k^z$. Note that the last term in equation (6) is equivalent to $\sum_k A_k (S_z + \frac{1}{2}\mathbb{1}_2) I_k^z$, where $S_z = (|1\rangle\langle 1| - |0\rangle\langle 0|)/2$, with $|0\rangle = |K'\downarrow\rangle$ ($|1\rangle = |K'\uparrow\rangle$) is the down (upper) state of the central spin. In fact, $S_z + \frac{1}{2}\mathbb{1}_2 = |1\rangle\langle 1|$. The transversal hyperfine term results in off-resonant transitions between the system and environmental spins, whereas the longitudinal hyperfine term provides additional contributions to the energy splitting.

The time evolution of the combined system, consisting of the electron spin and $\mathcal{N}$ nuclear spins, and given by the action of the total Hamiltonian $\mathcal{H}^I_{tot}$ in equation (6), is described in the following. (i) when $t < 0$ we assume that the electron spin and the nuclear system are decoupled, and both of them prepared independently in the states described by the density operators $\rho_S(0)$ and $\rho_E(0)$, respectively. (ii) At $t = 0$, the electron and nuclear spin system are brought into contact on a switching timescale $\tau_{sw} \ll 2\pi\hbar/|\omega_s - \omega_k + A|$ [21], which is sufficiently small, where $|\omega_s - \omega_k + A|$ is the largest energy scale in this problem. The state of the entire system,

described by the total density operator $\rho(t)$, where it's given at $t = 0$, $\rho(0) = \rho_S(0) \otimes \rho_E(0)$ with $\rho_S = \mathrm{Tr}_E(\rho)$ and $\rho_E = \mathrm{Tr}_S(\rho)$, this is called the reduced density matrix of the subsystem S and E, respectively. (iii) The evolution of the density operator $\rho(t)$ for $t \geqslant 0$ is governed by the Hamiltonian $\mathcal{H}^I_{tot}(t)$ for an electron spin coupled to an environment of nuclear spins.

This model is comparable to previous research investigations of an electron spin confined to a QD of Gallium arsenide (GaAs) [21] and graphene QD [22], but there are MoS_2 specific properties. Given that the natural abundance δ_i of spin-carrying isotopes is small for molybdenum Mo and sulfur S, hence only $\mathcal{N}$ of all atoms $\mathcal{N}_{tot}$ within the MoS_2 QD carry spin. However, in semiconducting materials such as GaAs, all isotopes possess a spin. To highlight these differences, we compare the most important characteristics of MoS_2, graphene, and GaAs, which are given in table 2. Indeed, the HI coupling constant A_{MoS_2}, is about approximately the same magnitude as $A_{Graphene}$ and it's about two orders of magnitude smaller than the constant A_{GaAs} in GaAs, which even further reduces the nuclear magnetic field by the same amount. Furthermore, the relatively small hyperfine energy $\mathcal{E}_{HF} = \hbar/\tau_{HF}$ (in the case of MoS_2 is on average of the order $\mathcal{E}_{HF} \approx 10^{-12}$ eV), in MoS_2 increases the timescale τ_{HF}. It also relies on both the hyperfine strength A and the isotopic abundance δ_i, of this interaction significantly compared to GaAs and graphene. The switching timescale τ_{sw} for various materials is also listed in table 2 as well.

Here, we drive into the method that used alongside with this work. We suppose at $t = 0$, that the total system, electron and nuclear, describe by

$$\psi(0) = \psi_S(0) \otimes \psi_E(0) \tag{7}$$

where $|\psi_S(0)\rangle$, is the initial state for the central spin and $|\psi_E(0)\rangle$ is the initial state for the nuclear spin bath where we start with a perfectly polarized nuclear ensemble, as shown in figure 1(b). Equation (7) can be written in the subspace spanned by the bases $\{|0\rangle \otimes |0\rangle_E, |1\rangle \otimes |0\rangle_E, |0\rangle \otimes (I_k^+|0\rangle_E)\}$ as follows,

$$|\psi(0)\rangle = c_0|0\rangle \otimes |0\rangle_E + c_1(0)|1\rangle \otimes |0\rangle_E + \sum_k c_k(0)|0\rangle \otimes (I_k^+|0\rangle_E) \tag{8}$$

where $|0\rangle_E = \otimes_k^{\mathcal{N}}|0\rangle = |0,\cdots,0\rangle$ denotes the vacuum state of the bath. Noting that, $c_k(0) = 0\ \forall\, k$. This means that the environment is initially in the vacuum state. Detailed calculations of the time evolution of the total system and the definition of the correlation function are provided in the appendix B. The correlation function in the continuum limit assumes the form $\int d\omega_k \mathcal{J}(\omega_k) e^{i(\omega_s + A_k/2 - \omega_k)(t-s)}$, with $\mathcal{J}(\omega_k) = \sum_k (A_k/2)^2 \delta(\omega_s - \omega_k)$ is the spectral density of the bath given by the sum of (coupling strength)^2 (density of modes), which is therefore simply the Fourier transform of the correlation function $\langle h^-(t)h^+(s)\rangle_E e^{i\omega_s(t-s)}$. The typical representative environments are described by the Lorentzian-type spectral functions, $\mathcal{J}(\omega_k) = \gamma_0 \lambda^2/2\pi((\omega_s - \omega_k)^2 + \lambda^2)$. Here, the parameter λ defines the width of the Lorentzian spectral density; in fact, it is the measure of memory capacity or non-Markovianity of the environment [51] and is related to the bath correlation time $\tau_E = 1/\lambda$. On the other hand, γ_0 measures the coupling strength between the qubit and its environment, and hence the characteristic time of the system $\tau_S = 1/\gamma_0$ denotes the relaxation time. Taking a Lorentzian spectral density in resonance with the qubit's transition frequency, we obtain an exponential two-point correlation function, denoted as

$$\langle h^-(t)h^+(s)\rangle_E e^{i\omega_s(t-s)} = \frac{1}{2}\gamma_0 \lambda \mathrm{e}^{-\lambda|t-s|} \tag{9}$$

We define the function $\tilde{G}(t) = G(t)e^{-iht}$, where $c_1(t) = G(t)c_1(0)$, which defined as the solution of the integro-differential equation,

$$\partial_t \tilde{G}(t) = -\int_0^t ds \langle h^-(t)h^+(s)\rangle_E e^{i\omega_s(t-s)} e^{-ih(t-s)} \tilde{G}(s) \tag{10}$$

with initial condition $\tilde{G}(0) = G(0) = 1$. Generally, $G(t)$ can be solved to give the exact solution by the Laplace transform. Indeed, substituting equation (9) into equation (10) we obtain the following

$$G(t) = e^{-\lambda t/2}\left(\frac{\sinh\left(\frac{\lambda\chi}{2}t\right)}{\chi} + \cosh\left(\frac{\lambda\chi}{2}t\right)\right) \tag{11}$$

where $\chi = \sqrt{1 - 2(\gamma_0/\lambda)}$. To get an ME in differential form with a generator local in time, we first provide the precise time evolution mapping [50], which transforms the initial states into the states at time t

$$\begin{aligned} \Phi(t)\colon \rho(0) \rightarrow \rho(t) &= \mathrm{Tr}_E\{|\psi(t)\rangle\langle\psi(t)|\} \\ &= \Phi(t)\rho(0),\ t \geqslant 0 \end{aligned} \tag{12}$$

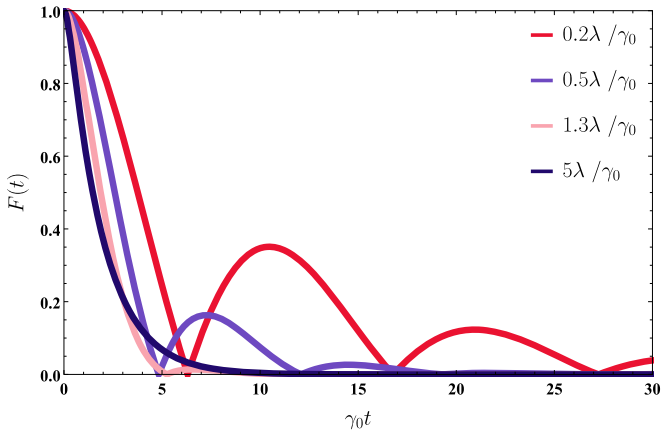

Figure 2. Time evolution of the fidelity $\mathcal{F}(t)$ in equation (15) using G(t) in equation (11), as a function of dimensionless time $\gamma_0\, t$ for different values of the environmental memory parameter λ/γ_0.

Then due to equation (B1), the density matrix $\rho(t)$ it is expressed as

$$\begin{aligned}\rho(t) &= \begin{pmatrix}\rho_{11}(t) & \rho_{10}(t)\\ \rho_{01}(t) & \rho_{00}(t)\end{pmatrix}\\ &= \begin{pmatrix}|G(t)|^2\rho_{11}(0) & G(t)\rho_{10}(0)\\ G^{\star}(t)\rho_{01}(0) & \rho_{00}(0)+(1-|G(t)|^2)\rho_{11}(0)\end{pmatrix}\end{aligned} \tag{13}$$

where $\rho_{ij}(t) = \langle i|\rho(t)|j\rangle$ for i, j = 0,1. We can construct the exact TCL equation by introduce a time-local generator $K_{\mathrm{TCL}}(t) = \dot{\Phi}(t)\Phi^{-1}(t)$ [50]. We can obtain an exact TCL ME to second order in the interaction picture [42, 51, 64, 65]

$$\begin{aligned}\partial_t\rho(t) &= K_{\mathrm{TCL}}(t)\rho(t)\\ &= -\frac{i}{2}\varepsilon(t)[S_+S_-,\,\rho(t)] + \gamma(t)\left[S_-\rho(t)S_+ - \frac{1}{2}\{S_+S_-,\,\rho(t)\}\right]\end{aligned} \tag{14}$$

The dynamics of the exact TCL ME, parameterized by $\epsilon(t) = -2\Im\left[\frac{\dot{G}(t)}{G(t)}\right]$, behave as a time-dependent Lamb shift caused by coupling with noisy surroundings, and $\gamma(t) = -2\Re\left[\frac{\dot{G}(t)}{G(t)}\right]$, behave as a time-dependent decay rate (decoherence rate). Furthermore, the decay rate $\gamma(t)$ might have negative values, indicating a significant non-Markovian tendency in the dynamics of the system [64]. We use the fidelity [51, 66] $\mathcal{F}(t) = \sqrt{\langle\psi(0)|\rho(t)|\psi(0)\rangle}$ to measure the decoherence dynamics of the central spin. Indeed, the coherence of spin qubits is highly affected by the nuclear spins of the host material and their hyperfine coupling to the electron spin. When the system is prepared in the initial state $|\psi(0)\rangle = |1\rangle$, the fidelity reads

$$\mathcal{F}(t) = \sqrt{|c_1(t)c_1(0)|^2} = |G(t)| \tag{15}$$

The fidelity depicted in figure 2, may be divided into two main regimes. In the weak-coupling case, which reflects that the decoherence dynamics of the quantum system is Markovian, $\lambda > 2\gamma_0$, one has $\chi \in \mathbb{R}$ ($\chi = \sqrt{1-2\gamma_0/\lambda}$) so that $G(t)$ is always positive. When there is no longer any exchange between the qubit and his surroundings, the coupling strength $\gamma_0 \to 0$ the fidelity $\lim_{\gamma_0\to 0}\mathcal{F}(t) \sim 1$. However, in the case of strong coupling, $\lambda < 2\gamma_0$ one has $\chi \in i\mathbb{R}$, so $G(t)$ oscillates between positive and negative values reaching zero. This means the fidelity $\mathcal{F}(t)$ will then decay with an oscillating. Indeed, for $\lambda/\gamma_0 < 1$, $\mathcal{F}(t)$ decays non-exponentially and displays a clear beating pattern as shown in figure 2, indicating that the quantum information flow bounces back from the spin bath to the qubit system as the fidelity lifetime lowers. This is the signature of non-Markovian behavior.

We analyze the scenario in which the central spin of a MoS_2-QD qubit overlaps with around $\mathcal{N}$ nuclear spins and interacts through HI. This may lead to entanglement between the qubit and the nuclear bath and to back-action effects from the qubit to the nuclei and vice versa. In this situation, we assume that the HI strength $A_k \approx A/\mathcal{N}$ and the nuclear Zeeman splitting $\omega_k = g_{I_k}\mu_N b_z$ satisfy a Gaussian distribution characterized by the mean value $\bar{\omega}$ and the parameter ν^2 is termed variance, where $\bar{\omega}$ and ν can be assumed to be of the same order as $\approx|A|/\sqrt{\mathcal{N}}$. Indeed, the electron Zeeman splitting $\omega_s \approx A = \mathcal{N}A_k \approx \sqrt{\mathcal{N}}\omega_k$ is much larger than nuclear splitting ω_k which can be approximated as a continuous variable centering around the average value $\sim A/\sqrt{\mathcal{N}}$ following Gaussian distribution, $\mathcal{P}(\omega) = 1/(\sqrt{2\pi}\,\nu)e^{-\frac{(\omega-\bar{\omega})^2}{2\nu^2}}$. The correlation function can be expressed as

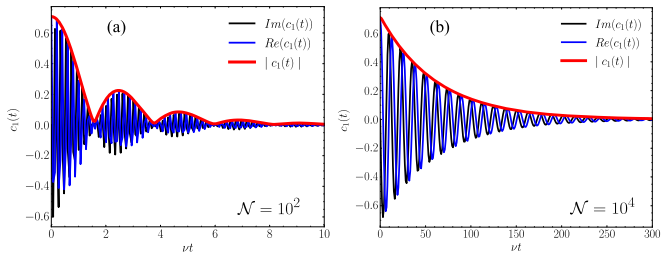

Figure 3. Time evolution of the amplitude $c_1(t)$ as a function of dimensionless time νt. Blue (black) lines: Real (imaginary) part of the amplitude $c_1(t)$. The initial state $|\psi(0)\rangle = \frac{1}{\sqrt{2}}(|0\rangle + |1\rangle)$, $c_0 = c_1(0) = 1/\sqrt{2}$. (a) we have $\mathcal{N} = 10^2$. (b) $\mathcal{N} = 10^4$.

follows,

$$\langle h^-(t)h^+(s)\rangle_E e^{i\omega_s(t-s)}e^{-ih(t-s)} = \sum_{k=0}^{\mathcal{N}-1}\left(\frac{A_k}{2}\right)^2 e^{i\Omega_k(t-s)} \tag{16}$$

where effective detuning $\Omega_k = \omega_s - \omega_k + A_k/2 - h$, is usually understood as a measure of memory capacity or non-Markovianity of the environment. Then, the effective correlation function of the spin bath can be evaluated as

$$\begin{aligned}\langle h^-(t)h^+(s)\rangle_E e^{i\omega_s(t-s)}e^{-ih(t-s)} &\approx \frac{A^2}{4N}e^{i(\omega_s+\frac{A}{2\mathcal{N}}-h)(t-s)} \times \int d\omega \mathcal{P}(\omega)e^{-i\omega(t-s)} \\ &\approx \frac{A^2}{4N}e^{-\frac{\nu^2}{2}(t-s)^2+i(\omega_s+\frac{A}{2\mathcal{N}}-h)(t-s)}\end{aligned} \tag{17}$$

The fidelity $\mathcal{F}(t)$ can be obtained numerically by inserting equation (17) into equation (10). To perform the numerical simulation, we selected the following MoS_2 parameters: The hyperfine coupling's strength has been estimated to be $A = 0.29\ \mu$ eV. This estimate is based on an average of the hyperfine coupling constants for the two nuclear isotopes ^{95}Mo and ^{97}Mo, weighted by their relative abundance. The naturally occurring isotopes carry spin with $I_{(^{95}\mathrm{Mo})} = I_{(^{97}\mathrm{Mo})} = 5/2$. In this model, we have the Overhauser field $h \approx I_0 A \approx \frac{5}{2}A$. Here, we study the case of a localized electron spin trapped in MoS_2-QD that interacts with $\mathcal{N}$ polarized nuclear spin environments via HI, where we employ the same TCL method as in some previous work [51].

Figures 3(a) and (b) depict the dynamics of $c_1(t)$ as a function of dimensionless time νt for various values of nuclear spins $\mathcal{N}$. Figure 3, for $\mathcal{N} = 10^2$, shows that the oscillation of the real and imaginary components of the amplitude $c_1(t)$ decays non-exponentially and displays a clear beating pattern. This oscillation eventually decreases with time to an equilibrium value. $|c_1(t)|$ shows nonmonotonic oscillatory decay with zero coherence revivals, which occurs by the electron spin-flip transition. Remarkably, the dynamics describes the initial oscillations of $c_1(t)$ appearing in the non-Markovian description of open quantum systems. However, figure 3(b) depicts the oscillation for $\mathcal{N} = 10^4$, where the decay rate of amplitude $c_1(t)$ increases significantly in comparison to figure 3(a) which depicts the transition from nonmonotonic oscillatory decay to monotonic decay. This indicates that increasing the number of nuclear spins $\mathcal{N}$ can decrease the quantum fluctuations caused by nuclear dynamics and boost the qubit's coherence.

To better understand how the environment of nuclear spins through HI affects the coherence of the MoS_2 qubit system, we analyze the temporal evolution of the density matrix $\rho(t)$. Figure 4 illustrate the evolution of populations (diagonal elements of the density matrix) and coherence (non-diagonal elements of the density matrix) as a function of dimensionless time νt. Figure 4(a) illustrates that the oscillation decays non-exponentially for non-diagonal elements and exhibits a distinct beating. These beating patterns clearly originate from the peaked nature of the environmental spectrum. The $\rho_{11}(t)$ shows nonmonotonic oscillatory decay with zero coherence revivals, which reflects that the decoherence dynamics of the quantum system is non-Markovian. However, by increasing the number of nuclear spins $\mathcal{N}$ and examining the figure 4(b), we can see that the non-diagonal elements exhibit a damped oscillatory behavior with the disappearance of the beat pattern. We can attribute this effect to the fact that when we increase $\mathcal{N}$, we go from a strong coupling regime between the qubit and the noisy environment described by the non-Markovian character to a weak coupling regime described by the Markovian character.

Figure 5 show the fidelity $\mathcal{F}(t)$ as a function of dimensionless time νt induced by the non-Markovian HI for different values of the number of nuclear spins $\mathcal{N}$ within the bath. The value of $\mathcal{F}(t)$ exactly reflects the decoherence of the central spin. The closer the value of $\mathcal{F}(t)$ to 1, the smaller the difference between the current state and the initial state of the central spin. As shown in figure 5 we can clearly see that when $\mathcal{N} = 10^2$, the fidelity shows nonmonotonic oscillatory decay with zero coherence revivals, meaning that the exchange of the

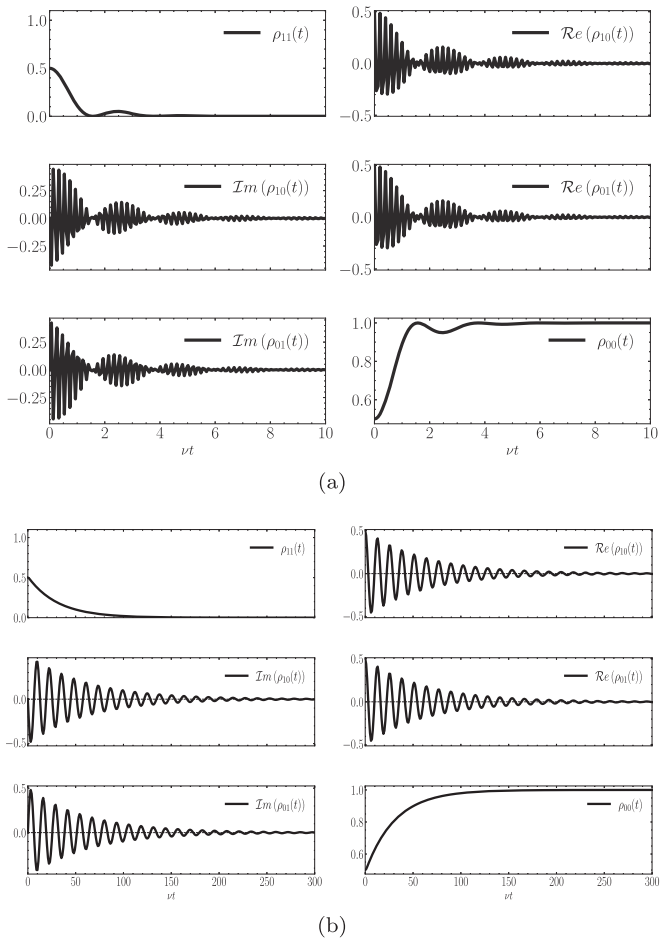

Figure 4. Time evolution of density matrix elements ρ_{ij} as a function of dimensionless time νt. We give results from the numerical equation (13). The initial state $|\psi(0)\rangle = \frac{1}{\sqrt{2}}(|0\rangle + |1\rangle)$, $c_0 = c_1(0) = 1/\sqrt{2}$. (a) Here, we have $\mathcal{N} = 10^2$. (b) Here, we have $\mathcal{N} = 10^4$.

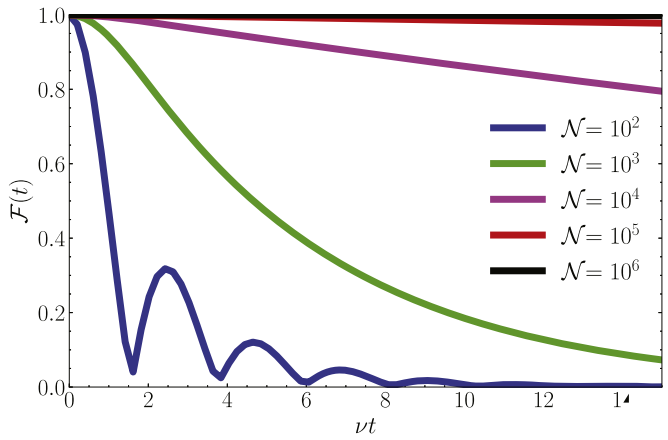

Figure 5. Time evolution of fidelity, $\mathcal{F}(t) = |\tilde{G}(t)|$ as a function of dimensionless time, νt, for different values of the number of nuclear spins within the bath $\mathcal{N}$. For a system is prepared in the initial state $|\psi(0)\rangle = |1\rangle$.

quantum information and energy between the system and bath spins having a noticeable or major effect, the quantum information flow bounces from the spin bath back to the system. On the contrary, when $\mathcal{N}$ increases, the decay rate of the central spin gradually decreases, as shown by the transition from nonmonotonic oscillatory decay to monotonic decay. In addition, the coherence of the central spin remains robust for large $\mathcal{N}$. These results indicate that the fidelity improves as the effect of environmental memory increases. The spin bath with $\mathcal{N}$ up to 10^6 ($R = 230$ nm) works as it provides natural protection for central spin coherence. For our qubit

scenario, the fidelity is represented in figure 5 with a solid purple line for $\mathcal{N} = 10^4$ ($R = 26$ nm). The varying of the nuclear spins $\mathcal{N}$ value depends on QD radius R as shown in appendix A, which mean by increasing R we increase $\mathcal{N}$. It is also important to know that selecting R is necessary for implementing the MoS_2 spin-valley qubit.

3. Conclusion and outlook

In this paper, we have proposed an exact ME for a central spin coupled to a spin bath via HI. We focus on the TCL ME for the full polarized environment bath. By studying an ML-MoS_2 spin valley QD with a perpendicular external magnetic field that can be used to tune the energy splitting between these two states. We analyze the decoherence dynamics of the induced noise determined by the correlation function corresponding to this spin-bath model, the uniform HI strength, and the Gaussian distribution in terms of the bath-spin frequency, respectively. Described by this noise, the effect of the spin bath on the central spin gives rise to a reduced dynamics. Furthermore, we have found that the Overhauser field in a QD system helps to restrict the decoherence process of the central electron spin, which can regain its coherence and retain its initial state in an environment with a larger number of bath spins. An obvious extension of this work is to use the fidelity to explicitly show the signature of non-Markovian behavior. As a consequence of this, the environmental non-Markovian feature can increase the coherence in the single-qubit dynamics. This model is qualitatively valid for other systems that satisfy the requirements of this later, where the most important demands are a Gaussian-like envelope function, slow dynamics of the nuclear bath, and sufficiently large Zeeman splitting with respect to the HI energy scale. The study of this qubit system in an unpolarized spin bath will be very interesting for future research, as it will allow us to see how the inhomogeneity of the hyperfine interaction affects the spin coherence and relaxation time.

Acknowledgments

This research has not received external funding.

Data availability statement

The data that support the findings of this study are available upon reasonable request from the authors.

Competing interests

The authors declare no conflicts of interest.

Appendix A. Choice of single electron QDs as spin qubits

Several methods and architectural designs have been proposed and tested experimentally to isolate a QD from TMD [67]. These include electrostatic gating [3, 9, 68–70], strain bubbles [71–73], nanoflakes [8, 63], lattice defects [74–78] or by forming potential wells with TMD lateral heterostructures [79]. Following the selection of a QD type, the next option for implementing a quantum processor in a TMD is a qubit space. The development of semiconductor nanostructures as low-noise hosts for qubits is a major undertaking. Understanding the band structure and external field replies is required for TMD monolayer (ML) to achieve qubits with carriers [3, 80]. However, the strong intrinsic spin-orbit coupling (SOC) [81, 82] within this TMD material has the opposite effect, making this a difficult task. Indeed, TMD is characterized by a significant splitting of the spin states ∼150 meV in the valence band (VB) [83, 84] and up to a few tens of meV in the conduction band (CB) [85–87] within the same valley K (K'), meaning that a single electron within a QD in TMD will not explain the required degeneracies wanted for a spin qubit. Favorably, the band crossing seen in the spin-resolved CB structures in ML-MoS_2 submit that is reasonable to accomplish spin degeneracy localized within a given valley K (K'), see figure 6(a). Consequently, such spin-degenerate regimes allow the possibility of realizing the desired qubits in the MoS_2-QD [3].

In particular, the band structure shown in figure 6(a) is calculated based on a self-consistent scheme, the present first principle study consists in solving the Kohn–Sham (KS) equations by using the all electron Full-Potential Linearized Augmented Plane Wave as embedded in a WIEN2k [88, 89] simulation package. The

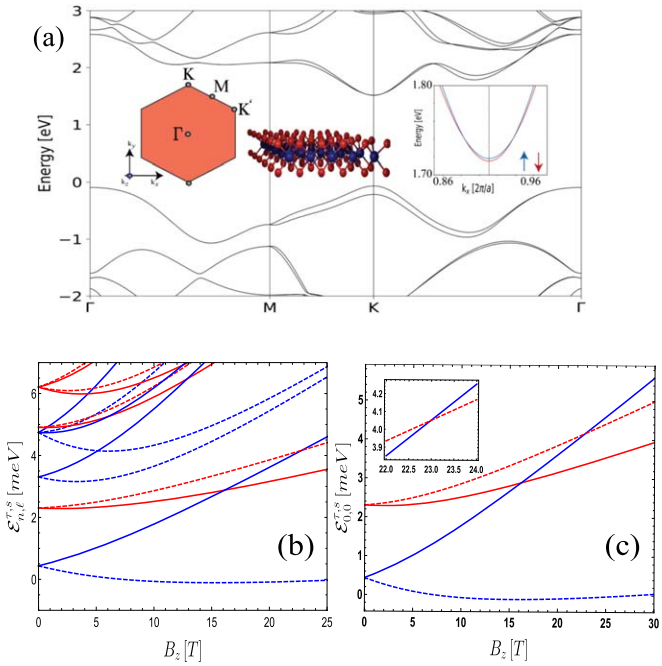

Figure 6. (a) Band structure of an ML-MoS_2 obtained from DFT calculations. Inset: First Brillouin zone (FBZ) with high symmetry k-path. Perspective view of ML-MoS_2. Blue and red balls represent the Mo and S atoms, respectively. The spin-resolved CB (red: $|0\rangle = |K'\downarrow\rangle$ and $|1\rangle_- = |K\uparrow\rangle$, blue: $|0\rangle_- = |K\downarrow\rangle$ and $|1\rangle = |K'\uparrow\rangle$) around the K valley in BZ demonstrating the spin crossings present in MoS_2, the K' valley can be visualized simply by the time-reversal of the given band structure. (b) Fock-Darwin Spectrum of a MoS_2-QD of radius $R = 26$ nm as a function of the perpendicular magnetic field B_z. Solid blue line (dotted): $|K'\uparrow\rangle$ ($|K\downarrow\rangle$) and continuous red line (dotted): $|K\uparrow\rangle$ ($|K'\downarrow\rangle$), respectively. The states up to $|\ell|$=1 and $n = 1$ are shown. (c) Part of the spectrum shown in (b) represent the ground state ($n = 0$, $\ell = 0$) energy spectra experience a perpendicular magnetic field B_z. Inset: region about which the twofold degeneracy localized to valley K' is observed in the spectrum of the two state $|K'\downarrow\rangle$ and $|K'\uparrow\rangle$.

Table 3. Effective masses, CB spin splitting, VB spin splitting, band gap energy (BG), valley and spin g-factor for ML-MoS_2 appearing in Hamiltonian (A1). m_e is the mass of the free electrons.

	Δ_{cb} [meV]	Δ_{vb} [meV]	$m_{eff}^{K,\uparrow}/m_e$	$m_{eff}^{K,\downarrow}/m_e$
MoS_2	2	145	0.54	0.49
	E_g[eV]	g_{vl}	g_{sp}	
	1.74	0.75 [3]	1.98 [3]	

generalized gradient approximation framework with a Perdew–Burke–Ernzerhof functional is used for the exchange correlation potential [90].

The eigenenergies of a single electron confined in a MoS_2-QD by the parabolic potential in a perpendicular magnetic field $\mathbf{B} = (0, 0, B_z)$, $B_z > 0$, about the valley K and K' can be obtained by solving the effective low-energy Hamiltonian [3]

$$\mathcal{H}_{B_z}^{\tau,s} = \frac{\hbar^2 \boldsymbol{P}_x^2}{2m_{eff}^{\tau,s}} + \frac{\hbar^2 \boldsymbol{P}_y^2}{2m_{eff}^{\tau,s}} + \frac{1}{2} m_{eff}^{\tau,s} \Omega_{\tau,s}^2 \, r^2 - \frac{1}{2} w_c^{\tau,s} \, \ell_z + \tau s \frac{\Delta_{cb}}{2} + \frac{1}{2} \tau g_{vl} \, \mu_B B_z + \frac{1}{2} s g_{sp} \, \mu_B B_z \tag{A1}$$

where $m_{eff}^{\tau,s}$ is the effective mass of the CB, see table 3.

τ and s denote the index, which takes the value $1(-1)$ indicated by the valley $K(K')$ and the spin $|\uparrow\rangle(|\downarrow\rangle)$, respectively. $\boldsymbol{P}_k = -i\boldsymbol{\partial}_k$ is the wave number operator, g_{vl} and g_{sp} is the valley and spin g-factor, ℓ_z is the z component of the orbital moment, μ_B is Bohr's magneton, and $\Omega_{\tau,s} = \sqrt{(\omega_0^{\tau,s})^2 + (\omega_c^{\tau,s}/2)^2}$ is the effective frequency, where $\omega_0^{\tau,s} = \hbar / (m_{eff}^{\tau,s} R^2)$ and $\omega_c^{\tau,s} = (eB_z)/(m_{eff}^{\tau,s})$ denote respectively the parabolic confinement and the cyclotron frequency. Here, R is the QD radius. Thus, the QD eigenvalues as a function of the out-of-plane magnetic field B_z and the QD radius R are given as

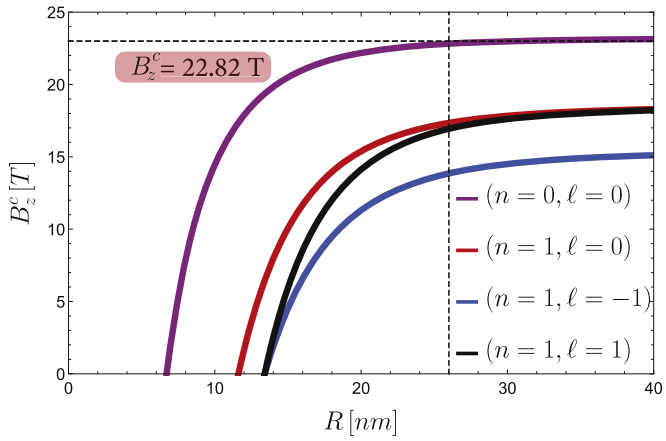

Figure 7. Spin-degeneracy curves of critical out-of-plane magnetic field B_z^c as function of MoS_2-QD radius R for the low-lying excited states; $(n=0,\ell=0)$, $(n=1,\ell=-1)$, $(n=1,\ell=0)$ and $(n=1,\ell=1)$.

$$\mathcal{E}_{n,\ell}^{\tau,s} = \hbar\,\Omega_{\tau,s}(2n+1+|\ell|) - \frac{1}{2}\hbar w_c^{\tau,s}\ell + \tau s\frac{\Delta_{cb}}{2} + \frac{1}{2}\tau g_{vl}\,\mu_B B_z + \frac{1}{2}s g_{sp}\,\mu_B B_z \tag{A2}$$

where n = 0, 1, …is the radial quantum number and $\ell = -\text{n}, -\text{n}+2, \ldots, \text{n}-2, \text{n}$ is the quantum number of the angular momentum. The wavefunction is given by $\psi_{n,\ell}^{\tau,s}(r,\ \phi) = A_{n,|\ell|}\frac{\exp(i\ell\phi)}{\sqrt{2\pi}}\left(\frac{m_{eff}^{\tau,s}\Omega_{\tau,s}}{2\hbar}r^2\right)^{|\ell/2|}\ \exp\left(-\frac{m_{eff}^{\tau,s}\Omega_{\tau,s}}{4\hbar}r^2\right)\times L_n^{|\ell|}\left(\frac{m_{eff}^{\tau,s}\Omega_{\tau,s}}{2\hbar}r^2\right)\chi_s(\sigma_z)$ with $A_{n,|\ell|}$ being the normalization coefficient and $L_n^{|\ell|}(x)$ being the associated Laguerre polynomials. $\chi_s(\sigma_z)$ is the eigenstate of the spin operator $S_z = \hbar\sigma_z/2$, where σ_z is the Pauli matrix. To obtain a qubit in a single TMD QD, a thoughtful selection of parameters is necessary to acquire some robustness. Therefore, by selecting the appropriate TMD type, QD size and perpendicular magnetic field a regime where $\mathcal{E}_{n,\ell}^{K(K'),\downarrow} = \mathcal{E}_{n,\ell}^{K(K'),\uparrow}$ may be achieved [9].

Figure 6 (b) shows the numerically calculated energy spectrum of the Fock-Darwin states for a MoS_2-QD. Figure 6(c) shows the energy spectra of the ground state ($n=0,\ \ell=0$). In the absence of a magnetic field, we have two separate states due to the two different effective masses of the electrons in QD. The magnetic field raises the degeneration of levels taking into account the degeneration of spin and valley, such that the eigenbasis is described by the Kramers pairs $|K'\uparrow\rangle$, $|K\downarrow\rangle$ and $|K\uparrow\rangle$, $|K'\downarrow\rangle$. The spin-valley Kramers space offers a range of qubit types that can be implemented in a QD: (i) Kramers qubit [4, 5, 63], in which the lowest lying Kramers pair is assumed to be the qubit space, i.e. $|0\rangle = |K,\downarrow\rangle$ and $|1\rangle = |K',\uparrow\rangle$. To isolate, such a qubit space requires only a minor influence from external magnetic fields. Gates with a Kramers qubit [5], on the other hand, are inherently slow because of the need for a spin and a valley flip to rotate between the two poles of the Kramers-Bloch sphere. (ii) Valley qubit [8, 63] that encodes the qubit in two states with different valleys but the same spin, i.e., $|0\rangle = |K,\uparrow\rangle$ and $|1\rangle = |K',\uparrow\rangle$. It takes the influence of an external B to raise the Kramers degeneracy in favor of a valley degeneracy, bringing these states energetically near enough together for efficient utilization as a qubit. However, these qubits need a slow valley mixing mechanism to perform gates using some defect-mediated process of nanoflake-type QDs [8]. (iii) Spin qubits [9] in various forms are a common type of qubit in conventional semiconductors [34, 91–95]. Within the same valley, it encodes the qubit in spin degree of freedom, i.e., $|0\rangle = |K',\downarrow\rangle$ and $|1\rangle = |K',\uparrow\rangle$. Because of their optically active direct BG, optically addressable spin states, and naturally low nuclear spin prevalence, TMD MLs should be an ideal spin-qubit platform. This article discusses our interest in spin qubits in TMD MLs. Indeed, figure 6(c) inset shows the regime where $\mathcal{E}_{n,\ell}^{K',\downarrow} = \mathcal{E}_{n,\ell}^{K',\uparrow} = 4.63$ meV for the critical magnetic field strength $B_z^c = 22.82$ T, which demonstrates spin-degenerate crosses for a given radius in the K' valley. This critical magnetic field B_z^c may be determined for a range of different QD radii to give the spin-degenerate regime $\mathcal{E}_{n,\ell}^{K',\downarrow} = \mathcal{E}_{n,\ell}^{K',\uparrow}$, shown in figure 7. Interestingly, for the QD radius $R \geqslant 26$ nm the value of B_z^c stabilizes to some equilibrium value for the ground state ($\text{n}=0, \ell=0$). Therefore, we assume $R = 26$ nm for the next step in this work. These spectra also show separate plateaus in the critical field strength at relatively high QD radii $R \geqslant 26$ nm between the ground state ($\text{n}=0, \ell=0$) and the first excited states ($\text{n}=0, \ell \geqslant 0$), differing by up to ~5 T.

By analyzing the ground state of a two-dimensional quantum system of electrons confined in a parabolic potential, we get the same results as the earlier work [3]. In this operating regime $\mathcal{E}_{n,\ell}^{K',\downarrow} = \mathcal{E}_{n,\ell}^{K',\uparrow}$, the spin-valley qubit's $|0\rangle = |K',\uparrow\rangle$ and $|1\rangle = |K',\downarrow\rangle$, states are degenerated. To achieve the Zeeman splitting for this qubit

space, we adjust the critical magnetic field with a value of $b_z \sim 1.5 \times 10^{-2}$ T. Theoretically, a TMD spin qubit has been demonstrated using an appropriate operational regime.

Appendix B. Time evolution of the total system

The time evolution of the total system, $t > 0$, can be written as the following expression,

$$|\psi(t)\rangle = c_0|0\rangle \otimes |0\rangle_E + c_1(t)|1\rangle \otimes |0\rangle_E + \sum_k c_k(t)|0\rangle \otimes (I_k^+|0\rangle_E) \tag{B1}$$

where we have used the normalization condition $|c_0|^2 + |c_1(t)|^2 + \sum_k |c_k(t)|^2 = 1$. Let us introduce the states: $|\psi_0\rangle = |0\rangle \otimes |0\rangle_E$, $|\psi_1\rangle = |1\rangle \otimes |0\rangle_E$ and $|\psi_k\rangle = |0\rangle \otimes |k\rangle_E$ where $|k\rangle_E = I_k^+|0\rangle_E = |0_1,\cdots,0_{k-1}, 1_k, 0_{k+1,\cdots}\rangle$ denotes the state with only one nuclear spin at site k. We can now express the time evolved state (B1) as $|\psi(t)\rangle = c_0|\psi_0\rangle + c_1(t)|\psi_1\rangle + \sum_k c_k(t)|\psi_k\rangle$. The amplitude c_0 is constant since $\mathcal{H}_{tot}^I(t)|\psi_0\rangle = 0$, while the amplitudes $c_1(t)$ and $c_k(t)$ are time-dependent. The time development of these amplitudes is governed by a system of differential equations which is obtained by the Hamiltonian $\mathcal{H}_{tot}^I$ in equation (6) and the Schrödinger equation, $i\partial_t|\psi(t)\rangle = \dot{c}_1(t)|\psi_1\rangle + \sum_k \dot{c}_k(t)|\psi_k\rangle$. Multiplying the Schrödinger equation by $\langle\psi_1|$ and $\langle\psi_k|$ gives us two coupled differential equations for the amplitudes $c_k(t)$ and $c_1(t)$

$$\begin{aligned}\frac{d}{dt}c_1(t) &= ihc_1(t) - i\sum_k \frac{A_k}{2}e^{i\left(\omega_s-\omega_k+\frac{A_k}{2}\right)t}c_k(t)\\ \frac{d}{dt}c_k(t) &= -i\frac{A_k}{2}e^{-i\left(\omega_s-\omega_k+\frac{A_k}{2}\right)t}c_1(t)\end{aligned} \tag{B2}$$

where $h = \langle h^z(t)\rangle = \langle\psi(t)|h_z|\ \psi(t)\rangle$. By integrating equation (B2), the coefficient $c_k(t)$ can be formally written as

$$c_k(t) = -i\frac{A_k}{2}\int_0^t ds\ e^{-i\left(\omega_s-\omega_k+\frac{A_k}{2}\right)s}c_1(s) \tag{B3}$$

Substituting it into equation (B2), we obtain an exact time-convolution dynamical equation for the central spin,

$$\frac{d}{dt}c_1(t) = ihc_1(t) - \int_0^t ds\,\langle h^-(t)h^+(s)\rangle_E\, e^{i\omega_s(t-s)}c_1(s) \tag{B4}$$

where $\langle h^-(t)h^+(s)\rangle_E e^{i\omega_s(t-s)} = \sum_k (A_k/2)^2 e^{i(\omega_s-\omega_k+A_k/2)(t-s)}$ is the associated memory kernel given by a two-point correlation function of the bath. $\langle\cdots\rangle_E$, is the expectation value on the environment state ρ_E, where $\rho_E(t) = (|0\rangle\langle 0|)_E$ is the vacuum state of the bath.

Appendix C. Hyperfine interaction Hamiltonian

The Hamiltonian describe an electron spin S immersed in a nuclear spin bath reads [59]

$$\mathrm{H} = \mathrm{H_S} + \mathrm{H_B} + \mathrm{H_{S-B}} \tag{C1}$$

where H_S and $\mathrm{H_B}$ are Hamiltonian for electron spin and nuclear spins, respectively, and H_{S-B} describes the qubit-bath interaction

$$\mathrm{H_S} = -g_{\mathrm{sp}}\mu_{\mathrm{B}}b_z S_z + \boldsymbol{S}\cdot\boldsymbol{D}\cdot\boldsymbol{S} \tag{C2}$$

$$\mathrm{H_B} = -\sum_k g_{I_k}\mu_{\mathrm{N}}b_z I_{z,k} + \mathrm{H_{n-n}} + H_Q \tag{C3}$$

$$H_{\mathrm{n-n}} = \frac{\mu_0}{4\pi}\sum_{i<j}\gamma_i\gamma_j\frac{\boldsymbol{I_i}\cdot\boldsymbol{I_j} - 3(\boldsymbol{I_i}\cdot\boldsymbol{r}_{ij})(\boldsymbol{I_j}\cdot\boldsymbol{r}_{ij})}{r_{ij}^3} \tag{C4}$$

$$\mathrm{H_{S-B}} = S_z\sum_k \boldsymbol{A_k}\cdot\boldsymbol{I_k} + H_{ahf} = \boldsymbol{h}\cdot\boldsymbol{S} + H_{ahf} \tag{C5}$$

where γ_i is the gyromagnetic ratio of the$i$th nucleus (see table 4 for numerical values of γ_i for Mo isotopes) and r_{ij} is the distance between the nuclear spins I_i and I_j. The first term in H_S represents the Zeeman interaction and the

Table 4. Values of quadrupole moments Q, quadrupole splitting ΔE_Q, Quadrupolar coupling constant, Asymmetry parameter and gyromagnetic ratios for some Molybdenum non-zero spin isotopes. Note that $1\ mb = 1.\times 10^{-31}\ \mathrm{m}^2$.

Molybdenum Isotopes	Q(mb)	$\Delta E_Q(\mu\mathrm{eV})$	eQV_{zz}(MHz)	η	$\gamma\,(10^7\ \mathrm{rad.T^{-1}.s^{-1}})$
^{95}Mo	−20.2 [97]	0.01	5.59	0	−1.75
^{97}Mo	250.5 [97]	0.14	69.36	0	−1.78

second term represents the zero-field splitting. The first term in H_B is the Zeeman term for the nuclei, the second term is the nuclear spin dipole-dipole interaction, while the last is the nuclear quadrupolar splitting. The first term in H_{S-B} Hamiltonian describing the interaction of a single electron S with the nuclei in the QD, while the second term describe the anisotropic hyperfine interaction.

C.1. Anisotropic hyperfine

The importance of nuclear-spin interactions strongly depends on the system under consideration. Indeed, the anisotropic hyperfine interaction [96]

$$H_{\text{ahf}} = \frac{\mu_0}{4\pi} 2\mu_B \gamma_N \frac{3(\mathbf{r}\cdot\mathbf{S})(\mathbf{r}\cdot\mathbf{I})/r - \mathbf{S}\cdot\mathbf{I}}{r^3} \tag{C6}$$

where **r** is the vector pointing from the nucleus to the electron, **S**(**I**) is the electron (nuclear) spin operator. This term is irrelevant for conduction-band electrons, where the hosted spin-valley qubit, because of the spherical symmetry of the orbital wavefunction [60, 96]. The anisotropic interaction become important when the electronic wavefunction have low symmetry.

C.2. Nuclear dipolar interaction

The dipole-dipole interaction between nuclear spins (e.g., ^{95}Mo and ^{97}Mo) is characterized by two factors: η and δ. η indicates the dipole-dipole interactions between nucleus i and j, which is given by equation (C4) ($H_{\text{n}-\text{n}}$). δ indicates the energy splitting between two levels interacting with $\boldsymbol{I}_i^+\boldsymbol{I}_j^- + \boldsymbol{I}_i^-\boldsymbol{I}_j^+$ due to the different Zeeman splitting with different nuclear spin g-factors between nuclei in addition to the dipole-dipole interaction between them. When $\delta \gg \eta$, the nuclear spins (^{95}Mo and ^{97}Mo) baths are decoupled, and the dipole-dipole interaction can be neglected. For instance, considering $\boldsymbol{I}_i^+\boldsymbol{I}_j^- + \boldsymbol{I}_i^-\boldsymbol{I}_j^+$ is the source of the decoherence induced by the dipole-dipole interaction, where we estimated the decoupling field [98]

$$B_{\text{dec}} = \frac{\mu_0\mu_N}{4\pi}\frac{1}{d^3}\frac{g_i g_j}{g_i + g_j} \tag{C7}$$

In MoS_2, the distance between molybdenum atom equal to d = 3.16 A [98], the nuclear g-factor for ^{95}Mo = − 0.3657, and the nuclear g-factor for ^{97}Mo = − 0.3734, this gives $B_{\text{dec}} = 0.28$mT. Since $B_{\text{dec}} = 0.28$mT much less than the Zeeman splitting b_z =15mT, thus the decoupling field suppresses the nuclear dipolar interactions. In this work, we consider the case where nuclear spins are perfectly polarized. In this case, the dipole-dipole interaction between nuclear spins becomes greatly suppressed [40, 96], so we can neglect the nuclear dipole-dipole term.

C.3. Nuclear quadrupolar splitting

The electric quadrupole interaction is associated with the non-spherical charge distribution around the nucleus. For a level of nuclear spin, I, the interaction between the quadrupole moment of the nucleus, Q, and the electric field gradient tensor V_{ii} with i = x, y and z is given by the Hamiltonian

$$H_Q = \frac{eQV_{zz}}{4I(2I-1)}[3\mathrm{I}_{\mathrm{z}}^2 - \mathrm{I}(\mathrm{I}-1) + \eta(\mathrm{I}_{\mathrm{x}}^2 - \mathrm{I}_{\mathrm{y}}^2)] \tag{C8}$$

with $\eta = \frac{|V_{xx} - V_{yy}|}{V_{zz}}$ is the asymmetry parameter. In this equation, V_{xx}, V_{yy} and V_{zz} are the non-zero electric field gradient tensor elements expressed with respect to the principal x, y and z axes and η is the electric field gradient tensor asymmetry parameter ($\eta = 0$ for axial asymmetry along the quantization axis z which is our case in MoS_2 since it belongs to the C_{3v} symmetry group, thus $V_{xx} = V_{yy}$. We employ the quantum espresso code [99] and the GIPAW formalism [100] to numerically estimate the values of the electric field gradient. To quantitatively estimate the effect of the quadrupole interaction, we calculate the induced energy splitting by this effect

$$\Delta E_Q = \frac{1}{2}eQV_{zz}\left(1 + \frac{1}{3}\eta^2\right)^{1/2} \tag{C9}$$

Values of the quadrupole moment Q and the quadrupolar splitting for the Mo isotopes are given in the table 4.

ORCID iDs

Mehdi Arfaoui https://orcid.org/0000-0001-7628-4159

References

[1] Lee J, Wang Z, Xie H, Mak K F and Shan J 2017 *Nat. Mater.* **16** 887
[2] Schaibley J R, Yu H, Clark G, Rivera P, Ross J S, Seyler K L, Yao W and Xu X 2016 *Nature Reviews Materials* **1**
[3] Kormanyos A, Zolyomi V, Drummond N D and Burkard G 2014 *Phys. Rev.*X **4** 011034
[4] David A, Burkard G and Kormányos A 2018 *2D Materials* **5**
[5] Széchenyi G, Chirolli L and Pályi A 2018 *2D Materials* **5** 035004
[6] Wu Y, Tong Q, Liu G-B, Yu H and Yao W 2016 *Phys. Rev.* B **93** 045313
[7] Pearce A J and Burkard G 2017 *2D Materials* **4** 025114
[8] Pawłowski J, Żebrowski D and Bednarek S 2018 *Phys. Rev.* B **97** 155412
[9] Brooks M and Burkard G 2017 *Phys. Rev.* B **95** 245411
[10] Yin Z, Li H, Li H, Jiang L, Shi Y, Sun Y, Lu G, Zhang Q, Chen X and Zhang H 2012 *ACS Nano* **6** 74
[11] Lee H S, Min S-W, Chang Y-G, Park M K, Nam T, Kim H, Kim J H, Ryu S and Im S 2012 *Nano Lett.* **12** 3695
[12] Wang G, Chernikov A, Glazov M M, Heinz T F, Marie X, Amand T and Urbaszek B 2018 *Rev. Mod. Phys.* **90** 021001
[13] Xia F, Wang H, Xiao D, Dubey M and Ramasubramaniam A 2014 *Nat. Photonics* **8** 899
[14] Perkins F K, Friedman A L, Cobas E, Campbell P M, Jernigan G G and Jonker B T 2013 *Nano Lett.* **13** 668
[15] Radisavljevic B, Whitwick M B and Kis A 2011 *ACS Nano* **5** 9934
[16] Wang H, Yu L, Lee Y-H, Shi Y, Hsu A, Chin M L, Li L-J, Dubey M, Kong J and Palacios T 2012 *Nano Lett.* **12** 4674
[17] Feierabend M, Berghäuser G, Knorr A and Malic E 2017 *Nat. Commun.* **8** 1
[18] Ma Q, Ren G, Xu K and Ou J Z 2021 *Adv. Opt. Mater.* **9** 2001313
[19] Mueller T and Malic E 2018 *npj 2D Materials and Applications* **2** 1
[20] Mak K F, Xiao D and Shan J 2018 *Nat. Photonics* **12** 451
[21] Coish W A and Loss D 2004 *Phys. Rev.* B **70** 195340
[22] Fuchs M, Rychkov V and Trauzettel B 2012 *Phys. Rev.* B **86** 085301
[23] Urbaszek B, Marie X, Amand T, Krebs O, Voisin P, Maletinsky P, Högele A and Imamoglu A 2013 *Rev. Mod. Phys.* **85** 79
[24] Ding W, Liu Y, Zheng Z and Chen S 2022 *Phys. Rev.* A **106** 012604
[25] Warburton R J 2013 *Nat. Mater.* **12** 483
[26] Chekhovich E, Makhonin M, Tartakovskii A, Yacoby A, Bluhm H, Nowack K and Vandersypen L 2013 *Nat. Mater.* **12** 494
[27] Xu J, Habib A, Kumar S, Wu F, Sundararaman R and Ping Y 2020 *Nat. Commun.* **11** 1
[28] Villazon T, Claeys P W, Polkovnikov A and Chandran A 2021 *Phys. Rev.* B **103** 075118
[29] Kurucz Z, Sørensen M W, Taylor J M, Lukin M D and Fleischhauer M 2009 *Phys. Rev. Lett.* **103** 010502
[30] Fernàndez-Acebal P *et al* 2018 *Nano Lett.* **18** 1882
[31] Gullans M, Krich J J, Taylor J M, Halperin B I and Lukin M D 2013 *Phys. Rev.* B **88** 035309
[32] Lai C W, Maletinsky P, Badolato A and Imamoglu A 2006 *Phys. Rev. Lett.* **96** 167403
[33] Merkulov I A, Efros A L and Rosen M 2002 *Phys. Rev.* B **65** 205309
[34] Hanson R, Kouwenhoven L P, Petta J R, Tarucha S and Vandersypen L M K 2007 *Rev. Mod. Phys.* **79** 1217
[35] Childress L, Dutt M V G, Taylor J M, Zibrov A S, Jelezko F, Wrachtrup J, Hemmer P R and Lukin M D 2006 *Science* **314** 281
[36] Hanson R, Dobrovitski V V, Feiguin A E, Gywat O and Awschalom D D 2008 *Science* **320** 352
[37] Taylor J M, Marcus C M and Lukin M D 2003 *Phys. Rev. Lett.* **90** 206803
[38] Goldstein G, Cappellaro P, Maze J R, Hodges J S, Jiang L, Sørensen A S and Lukin M D 2011 *Phys. Rev. Lett.* **106** 140502
[39] Cappellaro P, Goldstein G, Hodges J S, Jiang L, Maze J R, Sørensen A S and Lukin M D 2012 *Phys. Rev.* A **85** 032336
[40] Ding W, Zhang W and Wang X 2020 *Phys. Rev.* A **102** 032612
[41] Shirai Y, Hashimoto K, Tezuka R, Uchiyama C and Hatano N 2021 *Phys. Rev. Research* **3** 023078
[42] Klatt J, Kropf C M and Buhmann S Y 2021 *Phys. Rev. Lett.* **126** 210401
[43] Shibata F, Takahashi Y and Hashitsume N 1977 *J. Stat. Phys.* **17** 171
[44] Wenderoth S, Breuer H-P and Thoss M 2021 *Phys. Rev.* A **104** 012213
[45] Trevisan A, Smirne A, Megier N and Vacchini B 2021 *Phys. Rev.* A **104** 052215
[46] Colla A and Breuer H-P 2022 *Phys. Rev.* A **105** 052216
[47] Alipour S, Rezakhani A T, Babu A P, Mølmer K, Möttönen M and Ala-Nissila T 2020 *Phys. Rev.* X **10** 041024
[48] Vacchini B and Breuer H-P 2010 *Phys. Rev.* A **81** 042103
[49] Shen H Z, Qin M, Xiu X-M and Yi X X 2014 *Phys. Rev.* A **89** 062113
[50] Smirne A and Vacchini B 2010 *Phys. Rev.* A **82** 022110
[51] Jing J and Wu L-A 2018 *Sci. Rep.* **8** 1471
[52] Coish W A, Fischer J and Loss D 2008 *Phys. Rev.* B **77** 125329
[53] Chirolli L and Burkard G 2008 *Adv. Phys.* **57** 225
[54] Güldeste E T and Bulutay C 2022 *Phys. Rev.* B **105** 075202
[55] Cywiński L, Witzel W M and Sarma S Das 2009 *Phys. Rev.* B **79** 245314
[56] Tsyplyatyev O and Loss D 2011 *Phys. Rev. Lett.* **106** 106803
[57] Sinitsyn N A, Li Y, Crooker S A, Saxena A and Smith D L 2012 *Phys. Rev. Lett.* **109** 166605
[58] Schliemann J, Khaetskii A and Loss D 2003 *J. Phys. Condens. Matter* **15** R1809
[59] Ye M, Seo H and Galli G 2019 *NPJ Comput. Mater.* **5** 44
[60] Coish W and Baugh J 2009 *Phys. Status Solidi* B **246** 2203
[61] Avdeev I D and Smirnov D S 2019 *Nanoscale Adv.* **1** 2624
[62] Eng K *et al* 2015 *Science Advances* **1** e1500214
[63] Pawłowski J 2019 *New J. Phys.* **21** 123029
[64] Vacchini B and Breuer H-P 2010 *Phys. Rev.* A **81** 042103
[65] Tong Q-J, An J-H, Luo H-G and Oh C H 2010 *Phys. Rev.* A **81** 052330
[66] Jing J, Wu L-A, Sarandy M S and Muga J G 2013 *Phys. Rev.* A **88** 053422
[67] Davari S, Stacy J, Mercado A, Tull J, Basnet R, Pandey K, Watanabe K, Taniguchi T, Hu J and Churchill H 2020 *Phys. Rev. Applied* **13** 054058
[68] Zhang Z-Z *et al* 2017 *Science Advances* **3** e1701699
[69] Pisoni R, Lei Z, Back P, Eich M, Overweg H, Lee Y, Watanabe K, Taniguchi T, Ihn T and Ensslin K 2018 *Appl. Phys. Lett.* **112** 123101
[70] Song X-X *et al* 2015 *Nanoscale* **7** 16867

[71] Palacios-Berraquero C, Kara D M, Montblanch A R-P, Barbone M, Latawiec P, Yoon D, Ott A K, Loncar M, Ferrari A C and Atatüre M 2017 *Nat. Commun.* **8** 1
[72] Branny A, Kumar S, Proux R and Gerardot B D 2017 *Nat. Commun.* **8** 1
[73] Brooks M and Burkard G 2018 *Phys. Rev.* B **97** 195454
[74] Koperski M, Nogajewski K, Arora A, Cherkez V, Mallet P, Veuillen J-Y, Marcus J, Kossacki P and Potemski M 2015 *Nat. Nanotechnol.* **10** 503
[75] Tonndorf P, Schmidt R, Schneider R, Kern J, Buscema M, Steele G A, Castellanos-Gomez A, van der Zant H S J, de Vasconcellos S M and Bratschitsch R 2015 *Optica* **2** 347
[76] Srivastava A, Sidler M, Allain A V, Lembke D S, Kis A and Imamoğlu A 2015 *Nat. Nanotechnol.* **10** 491
[77] He Y-M *et al* 2015 *Nat. Nanotechnol.* **10** 497
[78] Chakraborty C, Kinnischtzke L, Goodfellow K M, Beams R and Vamivakas A N 2015 *Nat. Nanotechnol.* **10** 507
[79] Huang C, Wu S, Sanchez A M, Peters J J, Beanland R, Ross J S, Rivera P, Yao W, Cobden D H and Xu X 2014 *Nat. Mater.* **13** 1096
[80] Dias A C, Fu J, Villegas-Lelovsky L and Qu F 2016 *J. Phys. Condens. Matter* **28** 375803
[81] Zhu Z Y, Cheng Y C and Schwingenschlögl U 2011 *Phys. Rev.* B **84** 153402
[82] Wang G *et al* 2015 *Nat. Commun.* **6** 10110
[83] Zhang Y *et al* 2014 *Nat. Nanotechnol.* **9** 111
[84] Riley J M *et al* 2014 *Nat. Phys.* **10** 835
[85] Kormányos A, Burkard G, Gmitra M, Fabian J, Zólyomi V, Drummond N D and Fal'ko V 2015 *2D Materials* **2** 022001
[86] Liu G-B, Shan W-Y, Yao Y, Yao W and Xiao D 2013 *Phys. Rev.* B **88** 085433
[87] Kośmider K, González J W and Fernández-Rossier J 2013 *Phys. Rev.* B **88** 245436
[88] Blaha P, Schwarz K, Sorantin P and Trickey S 1990 *Comput. Phys. Commun.* **59** 399
[89] Blaha P *et al* 2001 An augmented plane wave+ local orbitals program for calculating crystal properties **60**
[90] Perdew J P, Chevary J A, Vosko S H, Jackson K A, Pederson M R, Singh D J and Fiolhais C 1992 *Phys. Rev.* B **46** 6671
[91] Loss D and DiVincenzo D P 1998 *Phys. Rev.* A **57** 120
[92] Petta J R, Johnson A C, Taylor J M, Laird E A, Yacoby A, Lukin M D, Marcus C M, Hanson M P and Gossard A C 2005 *Science* **309** 2180
[93] Russ M and Burkard G 2017 *J. Phys. Condens. Matter* **29** 393001
[94] Zwanenburg F A, Dzurak A S, Morello A, Simmons M Y, Hollenberg L C L, Klimeck G, Rogge S, Coppersmith S N and Eriksson M A 2013 *Rev. Mod. Phys.* **85** 961
[95] Awschalom D D, Bassett L C, Dzurak A S, Hu E L and Petta J R 2013 *Science* **339** 1174
[96] Fischer J, Trif M, Coish W and Loss D 2009 Solid State Communications *fundamental Phenomena and Applications of Quantum Dots* **149** 1443
[97] Stone N 2005 *At. Data Nucl. Data Tables* **90** 75
[98] Kanai S, Heremans F J, Seo H, Wolfowicz G, Anderson C P, Sullivan S E, Onizhuk M, Galli G, Awschalom D D and Ohno H 2022 *Proceedings of the National Academy of Sciences* 119 e2121808119
[99] Giannozzi P *et al* 2009 *J. Phys. Condens. Matter* **21** 395502
[100] Pickard C J and Mauri F 2002 *Phys. Rev. Lett.* **88** 086403